Simulation of crack propagation in functionally graded materials under mixed-mode and non-proportional loading

JEONG-HO KIM and GLAUCIO H. PAULINO*

Department of Civil and Environmental Engineering, University of Illinois at Urbana-Champaign, Newmark Laboratory, 205 North Mathews Avenue, Urbana, IL 61801, USA
*Author for correspondence (E-mail: paulino@uiuc.edu; Phone: +1-217-333-3817; Fax: +1-217-265-8041)

Abstract. Automatic simulation of crack propagation in homogeneous and functionally graded materials is performed by means of a remeshing algorithm in conjunction with the finite element method. The crack propagation is performed under mixed-mode and non-proportional loading. Each step of crack growth simulation consists of calculation of mixed-mode stress intensity factors by means of a novel formulation of the interaction integral method, determination of crack growth direction based on a specific fracture criterion, and local automatic remeshing along the crack path. The present approach requires a user-defined crack increment at the beginning of the simulation. Crack trajectories obtained by the present numerical simulation are compared with available experimental results.

Key words: functionally graded material (FGM), fracture mechanics, stress intensity factors, interaction integral, two-state integral, finite element method (FEM), automatic crack propagation

1. Introduction

Functionally graded materials (FGMs) are new multifunctional composites with smoothly varying volume fractions of constituent materials, which leads to a non-uniform microstructure with continuously graded macroproperties (Hirai, 1993; Suresh and Mortensen, 1998; Paulino et al., 2003). FGMs possess material non-homogeneity with regard to thermomechanical and strength related properties including fracture toughness, yield strength, fatigue and creep behavior. These materials were introduced to take advantage of ideal behavior of its material constituents. For instance, partially stabilized zirconia (PSZ) shows a high resistance to heat and corrosion, and CrNi alloy has high mechanical strength and toughness (Ilschner, 1996), which is illustrated in Figure 1.

As the manufacturing of FGMs advances, knowledge of the behavior of cracks in FGMs becomes very important for assessing and enhancing structural integrity. In this paper, crack growth in both homogeneous and functionally graded materials is investigated and simulated by means of a remeshing algorithm in conjunction with the finite element method considering mixed-mode (I and II) and non-proportional loading.

The fracture parameters describing the crack tip fields in linear elastic FGMs include stress intensity factors (SIFs), which are important for determining crack growth direction under mixed-mode loading conditions. The mixed-mode SIFs (both K_I and K_{II}) in FGMs are functions of material gradients, external loading and geometry (see, for example, Kim and Paulino, 2002a). The material gradients do not affect the order of singularity and the angular functions of the singular crack-tip fields, but do affect the SIFs (Eischen, 1987). The correspondence of the crack-tip behavior between homogeneous and compositionally graded materials provides a
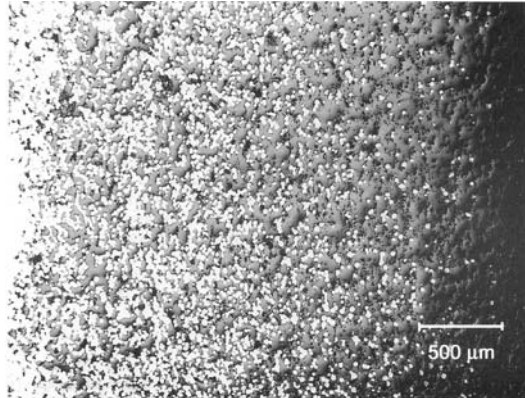
Figure 1. Micrograph illustrating graded transition region between CrNi alloy and PSZ (after Ilschner, 1996).

basis for *local homogenization* near the crack tip (see Figure 2), as discussed by Gu and Asaro (1997).

Based on the assumption that the graded material is locally homogeneous near the crack tip, this paper establishes the relationship between the asymptotically defined interaction integral (M-integral) and SIFs, converts the M-integral to an equivalent domain integral (EDI) using auxiliary fields, calculates SIFs using a finite domain, and predicts crack growth direction by extending a fracture criterion originally developed for homogeneous materials. In this paper, we use the maximum energy release rate criterion (Hussain et al., 1974) to check crack initiation condition and to determine crack initiation angles (Kim, 2003). Crack increment also has an effect on simulation of crack growth. The present approach is based on a user-defined crack increment, which is provided at the beginning of each step.

The contribution of this paper includes the numerical simulation of mixed-mode crack propagation in FGMs, and accurate evaluation of mixed-mode SIFs in FGMs using a novel interaction integral method, which accounts for material non-homogeneity effects. The remainder of this paper is organized as follows. The next subsection presents a motivation to this work. Next, a brief literature review and comments on previous related work are presented. Section 2 presents details of automatic crack propagation in FGMs including finite element mesh generation and a
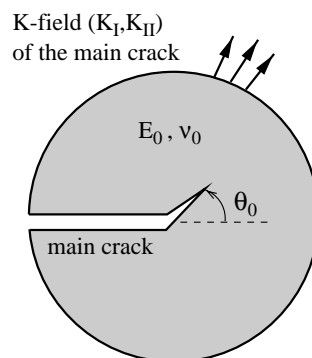

Figure 2. Local homogenization near the crack tip in an FGM. A locally homogenized material is subjected to the K-field (K_I, K_{II}) of the main crack.
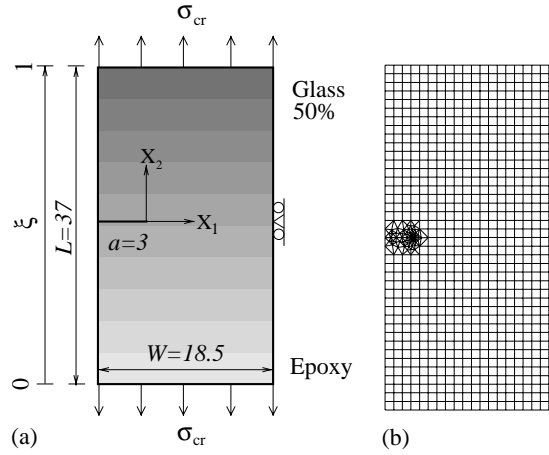
Figure 3. Motivation: FGM plate (units: N, mm): (a) geometry and boundary conditions; (b) the complete FEM mesh.

remeshing algorithm. Section 3 presents the interaction integral method for evaluating SIFs in FGMs. Section 4 presents a fracture criterion and its extension to FGMs. Section 5 provides numerical examples on simulation of crack propagation in FGMs. Finally, Section 6 presents concluding remarks and potential extensions of this work.

1.1. MOTIVATION

Compared to standard composite materials, FGMs may offer potential advantages such as reduction of residual stress (Lee and Erdogan, 1995), increased bonding strength (Kurihara et al., 1990), and reduction of stress concentration or stress intensity factors (Erdogan, 1995; Kim and Paulino, 2002b). Material non-homogeneity has a significant influence on SIFs, which in turn will influence subsequent crack trajectory (Kim, 2003). *For instance, under mode-I symmetric loading conditions, a crack in FGMs with material gradation perpendicular to the crack line tends to deviate from the projected path parallel to the crack line, as illustrated below.* In this case, the stronger the material variation, the more the crack deviates.

To motivate the present work, let's consider the FGM plate of Figure 3(a). The plate has 6 mm thickness, and it is subjected to tension loads, i.e. σ_{cr} (MPa), on the top and bottom edges. The critical load σ_{cr} is defined as the load required to propagate the crack at each step of crack propagation. Here we consider a state of plane stress. The basic FGM constituents adopted here

Table 1. Material properties (Young's modulus E, Poisson's ratio v, and fracture toughness K_{Ic}) at interior points in the graded region

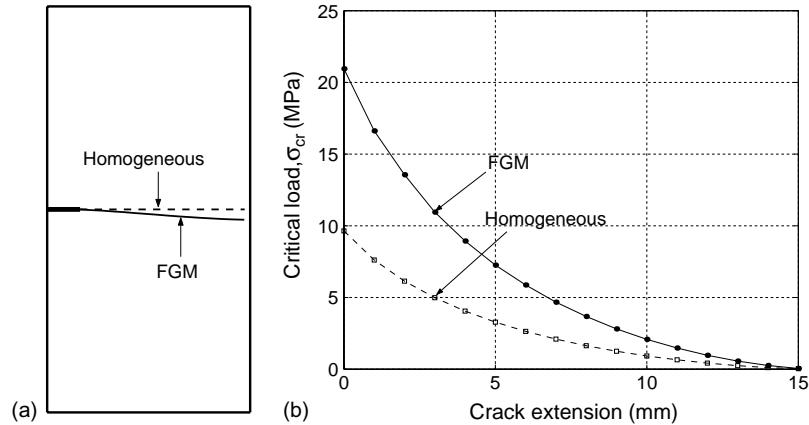| ξ	E (MPa)	v	K_{Ic} (MPa$\sqrt{m}$)
0.00	3000	0.35	1.2
0.17	3300	0.34	2.1
0.33	5300	0.33	2.7
0.58	7300	0.31	2.7
0.83	8300	0.30	2.6
1.00	8600	0.29	2.6

Figure 4. Motivation: comparison of numerical results between homogeneous and epoxy/glass FGM plates: (a) crack trajectories ($\Delta a = 1$ mm); (b) critical loads versus crack extension. The stronger the material gradient the bigger the crack deviation effect.

are epoxy and glass with volume fraction 50%, which were fabricated by Rousseau and Tippur (2000). The numerical values of material properties in the graded region ($0 \leq \xi \leq 1$) are illustrated in Table 1. Young's modulus and Poisson's ratio vary with the Cartesian coordinate X_2 (see Figure 3(a)). For the homogeneous case, material properties for epoxy are used. Figure 3(b) shows the FEM mesh for the plate. The mesh discretization consists of 818 eight-node quadrilateral (Q8) elements, 106 six-node triangular (T6) elements, and 12 six-node quarter-point triangular (T6qp) elements, with a total of 936 elements and 2827 nodes.

Figure 4(a) shows comparison of crack trajectory for the homogeneous plate with that for the graded plate obtained by the interaction integral method and the maximum energy release rate criterion considering the crack extension increment $\Delta a = 1$ mm (constant). For the homogeneous case, as expected, the crack grows along the direction parallel to the crack line because of symmetry ($K_{II} = 0$), however, for the FGM case, the crack turns to the lower (compliant) side of the plate due to material gradation, i.e., $K_{II} > 0$. Figure 4(b) shows comparison of critical loads σ_{cr} for the homogeneous plate with those for the graded plate obtained by the present numerical simulation. Notice that the critical loads (σ_{cr}) in all the steps for the FGM plate are greater than those for the homogeneous plate. This is due to increased fracture toughness for the FGM plate. Thus crack initiation is delayed due to material gradation. In summary, this example shows that material non-homogeneity has a significant influence on crack trajectory and critical loads required to propagate the crack. Moreover, if properly used, FGMs can delay crack initiation.

1.2. RELATED WORK

Accurate determination of SIFs in FGMs is crucial for predicting crack initiation and direction of propagation. The interaction integral method is an accurate and robust scheme for evaluating SIFs in FGMs. For instance, Dolbow and Gosz (2002) considered the plane problem of an arbitrarily oriented crack and used the extended finite element method (X-FEM), Rao and Rahman (2003) used the element-free Galerkin (EFG) method, and Kim and Paulino (2003a, b) used the FEM to investigate cracked FGMs with material properties determined by means of either continuum functions (e.g., exponentially graded materials) or micromechanics models

(e.g., self-consistent or Mori–Tanaka method). For the reasons described above, the interaction integral method is chosen for this work.

Gu and Asaro (1997) investigated crack deflection in brittle FGMs by considering exponential gradation perpendicular to the crack, and used the $K_{II} = 0$ criterion (Cotterell and Rice, 1980). They investigated the effect of material non-homogeneity on kink angles for three-point bending, double cantilever, four-point bending, and center-cracked specimens. Becker et al. (2001) investigated finite crack kinking by considering a hyperbolic-tangent material gradation with steep gradient of Young's modulus. They used the maximum energy release rate (Palaniswamy and Knauss, 1978) and $K_{II} = 0$ (Cotterell and Rice, 1980) criteria. On the other hand, there are an increasing number of fracture experiments on crack growth in FGMs in the literature. Lin et al. (1994) investigated mode I fracture of aluminium alloy 2124/SiC FGMs where the crack is parallel to material gradation. Moon et al. (2002) investigated crack growth resistance (R-curve) behavior of multilayer graded alumina–zirconia FGMs considering a crack parallel to the material gradation. Carpenter et al. (1999) performed fracture testing and analysis of a layered functionally graded Ti/TiB beam subjected to three-point bending. Rousseau and Tippur (2000) investigated crack kink angles and crack growth for a crack normal to the material gradient in FGM beams (made of solid A-glass spheres dispersed within a slow curing epoxy matrix) subjected to four-point bending. Lambros et al. (2000) and Abanto-Bueno and Lambros (2002) investigated mode I crack growth for an edge crack in FGMs subjected to fixed-grip loading. The FGMs were fabricated using a polyethylene 1% carbon monoxide co-polymer (ECO) which was subjected to controlled ultraviolet (UV) irradiation time throughout the specimen. Recently, Kim (2003) performed numerical simulation of mixed-mode crack propagation in FGMs, and investigated the effect of material gradation on crack trajectory and critical loads.

2. Automatic crack propagation in FGMs

Automatic crack propagation in FGMs is performed by means of the I-FRANC2D (Illinois-FRANC2D) code, an interactive graphics program for simulating 2D fracture analysis. The crack representation is based on the discrete crack approach. The present code is based on FRANC2D (FRacture ANalysis Code 2D) (Wawrzynek, 1987; Wawrzynek and Ingraffea, 1991), which was originally developed at Cornell University. The extended capabilities of I-FRANC2D consist of special graded elements to model non-homogeneous materials (see Figure 5), and fracture parameters for FGMs (such as SIFs) which are used to determine crack
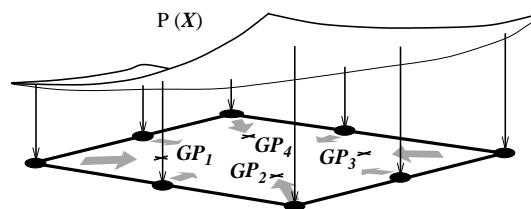

Figure 5. Generalized isoparametric formulation (GIF) (Kim and Paulino, 2002a, b) using graded finite elements. The above figure illustrates a graded Q8 element and $P(X)$ denotes a generic material property. The material properties at the Gauss points (P_{GP}) are interpolated from nodal material properties (P_i) by $P_{GP} = \sum N_i P_i$ where N are element shape functions.
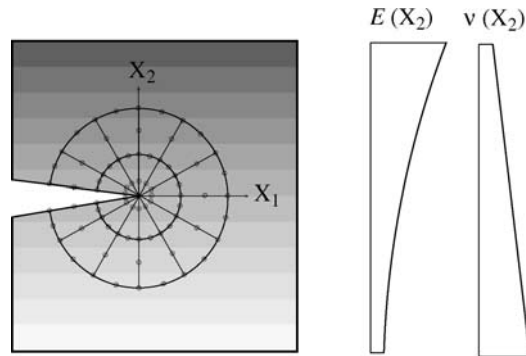
Figure 6. Crack-tip discretization for a crack in a non-homogeneous material.

initiation and to predict crack initiation angles. The I-FRANC2D code uses graded quarter-point six-node triangular (T6qp) elements to capture the stress singularity of $O(r^{-1/2})$, and it can perform mesh refinement around the crack tip in both radial (rings) and hoop (sectors) directions for each step of crack propagation (see Figure 6).

The basic framework for finite element simulation of automatic crack propagation in the I-FRANC2D code is identical to that of FRANC2D, and it involves successive steps. Each step consists of an automatic crack propagation cycle as illustrated in Figure 7. The I-FRANC2D code uses the standard direct stiffness approach of the FEM within the framework of linear elasticity. After the linear analysis involving a crack is performed, the code computes mixed-mode SIFs with high accuracy using the interaction integral method. The computed SIFs are used to check crack initiation condition by comparison with fracture toughness function, and are also used to predict crack growth direction based on a fracture criterion (e.g. maximum energy release rate). When the new crack tip location is determined according to the user-defined crack increment, the code deletes elements along the incremental crack path, updates crack geometry, and performs automatic local remeshing.

2.1. FINITE ELEMENT MESH GENERATION

Discrete crack growth analysis requires modification of the FEM mesh at each step of crack propagation. The geometry update of crack propagation is modeled based on the winged-edge
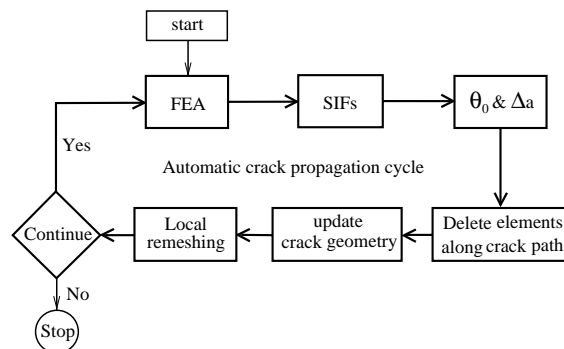

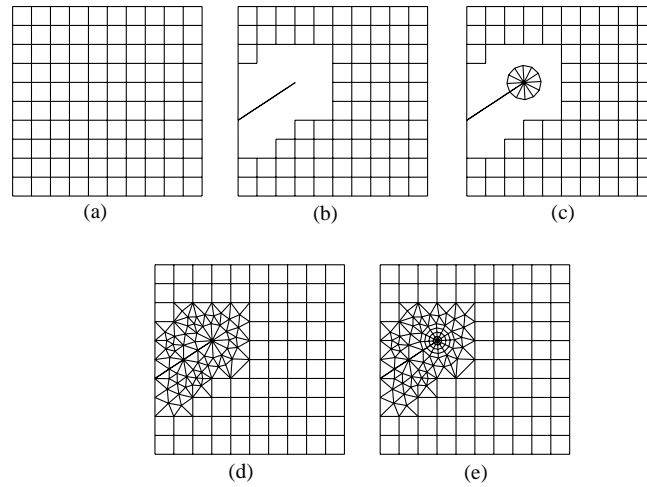*Figure 7.* Automatic crack propagation cycle used in the I-FRANC2D code.

Figure 8. Sequential procedure for geometry updating and remeshing (Bittencourt et al., 1996): (a) initial geometry; (b) deletion of nearby elements and construction of crack geometry; (c) meshing of singular crack-tip elements; (d) meshing of transition elements; (e) local refinement of crack-tip elements.

data structure (Wawrzynek, 1987), which uses the FEM mesh topology such as vertices, edges and faces. Figure 8 illustrates the procedure for local remeshing. The remeshing sequence is as follows (Bittencourt et al., 1996):

- Crack geometry is identified by the user in the initial geometrical configuration (see Figure 8(a)).
- A remeshing region is created by deleting elements near the crack in the polygon pattern, and the crack geometry is updated (see Figure 8(b)).
- Quarter-point six-node triangular (T6qp) elements are created around the crack tip (see Figure 8(c)).
- Triangular elements are generated by a triangulation algorithm (see Figure 8(d)).
- The local mesh refinement is done around the crack tip by increasing the number of elements in the radial and hoop directions (see Figure 8(e)).

2.2. REMESHING ALGORITHM

An algorithm for performing automatic crack propagation should satisfy two conditions (Bittencourt et al., 1996). First, the algorithm should keep compatibility between the new mesh and the existing mesh. Second, the algorithm should generate well-shaped elements with good aspect ratios, especially in the transition zone between the crack-tip and the far-field regions.

The present remeshing algorithm used in I-FRANC2D is the recursive spatial decomposition (RSD) algorithm, which was originated in the code FRANC2D (Wawrzynek, 1987; Wawrzynek and Ingraffea, 1991). The algorithm takes a region and subdivide it into smaller regions. The current algorithm uses the quadtree and the boundary-contraction scheme. The procedure for the overall remeshing algorithm is as follows (see Figure 9) (Bittencourt et al., 1996):

- The geometry data on the boundary, i.e. nodes and edges, are given (see Figure 9(a)).
- The quadtree configuration is generated. The given boundary data is used to determine a local subdivision level (see Figure 9(b)).
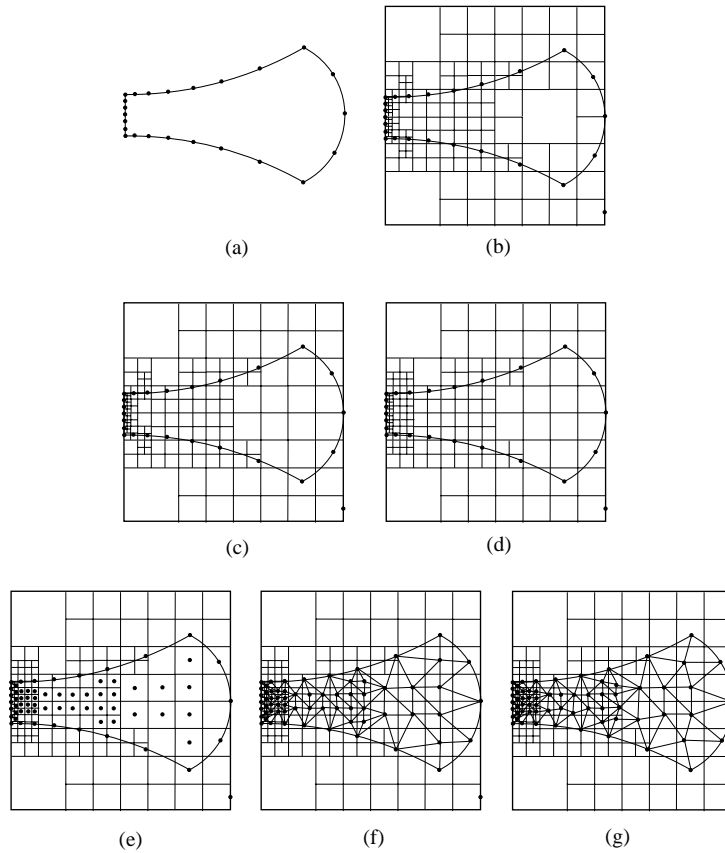
Figure 9. Procedure for RSD remeshing (Bittencourt et al., 1996): (a) input of boundary nodes and edges; (b) initial quadtree subdivision; (c) minimum subdivision of interior cells; (d) graded subdivision; (e) internal nodes generated at the center of the cells; (f) elements generated before smoothing; (g) elements generated after smoothing.

- The quadtree is refined to make interior cells smaller than the largest cell around the boundary (see Figure 9(c)).
- The quadtree is additionally refined to minimize the size difference between adjacent cells (see Figure 9(d)).
- Internal nodes are generated at the center of the quadtree cells (see Figure 9(e)).
- A boundary-contraction procedure is used to produce a trial mesh. (see Figure 9(f)).
- The size and shape of neighboring elements is regularized by moving internal nodes to the centroid of the adjacent nodes (see Figure 9(g)).

It is worth mentioning that the above techniques have also been used by Paulino et al. (1999) and extended to self-adaptive finite element analysis using the *h*-version of the FEM.

3.   The interaction integral for FGMs: stress intensity factors

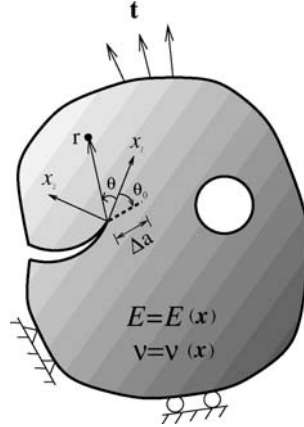The singular stress fields around the crack tip in FGMs take the form (Eischen, 1987) (see Figure 10)

Figure 10. Cartesian (x_1, x_2) and polar (r, θ) coordinates originating from the crack tip in an arbitrary FGM under traction (**t**) and displacement boundary conditions. The crack initiation angle is θ_0, and Δa denotes the crack extension.

$$\sigma_{ij}(r, \theta) = \frac{K_{\mathrm{I}}}{\sqrt{2\pi r}} f_{ij}^{\mathrm{I}}(\theta) + \frac{K_{\mathrm{II}}}{\sqrt{2\pi r}} f_{ij}^{\mathrm{II}}(\theta), \tag{1}$$

where σ_{ij} denotes the stress tensor, K_{I} and K_{II} are the mode I and mode II SIFs, respectively, and the angular functions $f_{ij}(\theta)$ can be found in several references, e.g. Eftis et al. (1977).

SIFs are important fracture parameters to characterize crack behavior. In this paper, we use the interaction integral (M-integral[1]) method to evaluate SIFs in FGMs. The auxiliary fields and the relationship between SIFs and M-integral are explained below.

3.1. AUXILIARY FIELDS

The interaction integral uses auxiliary fields, such as displacements ($\boldsymbol{u}^{\mathrm{aux}}$), strains ($\boldsymbol{\varepsilon}^{\mathrm{aux}}$), and stresses ($\boldsymbol{\sigma}^{\mathrm{aux}}$). These auxiliary fields have to be suitably defined in order to evaluate mixed-mode SIFs. There are various choices for the auxiliary fields. Here a non-equilibrium formulation is adopted, which uses displacement and strain fields developed for homogeneous materials, and employs the non-equilibrium stress fields given by (Kim, 2003).

$$\boldsymbol{\sigma}^{\mathrm{aux}} = \boldsymbol{C}(\boldsymbol{x})\boldsymbol{\varepsilon}^{\mathrm{aux}}, \tag{2}$$

where $\boldsymbol{C}(\boldsymbol{x})$ is the stiffness tensor. The auxiliary displacement and strain fields are chosen as (Williams, 1957):

$$\boldsymbol{u}^{\mathrm{aux}} = \frac{K_{\mathrm{I}}}{\mu_{\mathrm{tip}}} \sqrt{\frac{r}{2\pi}} \boldsymbol{g}^{\mathrm{I}}(\theta) + \frac{K_{\mathrm{II}}}{\mu_{\mathrm{tip}}} \sqrt{\frac{r}{2\pi}} \boldsymbol{g}^{\mathrm{II}}(\theta), \tag{3}$$

$$\boldsymbol{\varepsilon}^{\mathrm{aux}} = (\mathrm{sym}\nabla)\boldsymbol{u}^{\mathrm{aux}}, \tag{4}$$

where $K_{\mathrm{I}}^{\mathrm{aux}}$ and $K_{\mathrm{II}}^{\mathrm{aux}}$ are the auxiliary mode I and mode II SIFs, respectively, and μ_{tip} is the shear modulus at the crack tip. The representative functions $\boldsymbol{g}^{\mathrm{I}}(\theta)$ and $\boldsymbol{g}^{\mathrm{II}}(\theta)$ can be found in many references, e.g. Eftis et al. (1977).

---

[1]Here, the so-called M-integral should not be confused with the M-integral (conservation integral) of Knowles and Sternberg (1972), Budiansky and Rice (1973), and Chang and Chien (2002). Also, see the book by Kanninen and Popelar (1985) for a review of conservation integrals in fracture mechanics.
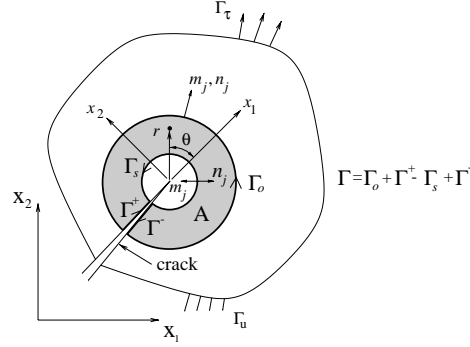
Figure 11. Conversion of the contour integral into an EDI. Here $\Gamma = \Gamma_o + \Gamma^+ - \Gamma_s + \Gamma^-$, $m_j = n_j$ on Γ_o and $m_j = -n_j$ on Γ_s.

3.2. FORMULATION OF THE INTERACTION INTEGRAL FOR FGMS

The interaction integral is derived from the path-independent *J*-integral (Rice, 1968) for two admissible states of a cracked elastic FGM body. The standard *J*-integral is given by

$$J = \lim_{\Gamma_s \to 0} \int_{\Gamma_s} (\mathscr{W} \delta_{1j} - \sigma_{ij} u_{i,1}) \, n_j \, d\Gamma, \tag{5}$$

where $\mathscr{W}$ is the strain energy density expressed by $\mathscr{W} = \sigma_{ij}\varepsilon_{ij}/2$ and n_j is the outward normal vector to the contour Γ_s, as shown in Figure 11. Applying the divergence theorem and using the weight function q, the EDI is obtained as

$$J = \int_A (\sigma_{ij} u_{i,1} - \mathscr{W} \delta_{1j}) \, q_{,j} \, dA + \int_A (\sigma_{ij} u_{i,1} - \mathscr{W} \delta_{1j})_{,j} \, q \, dA. \tag{6}$$

The *J*-integral of the superimposed fields (actual and auxiliary fields) is decomposed into

$$J^s = J + J^{\text{aux}} + M \tag{7}$$

where J^{aux} is given by

$$J^{\text{aux}} = \int_A (\sigma_{ij}^{\text{aux}} u_{i,1}^{\text{aux}} - \mathscr{W}^{\text{aux}} \delta_{1j}) \, q_{,j} \, dA + \int_A \left\{ \sigma_{ij}^{\text{aux}} u_{i,1}^{\text{aux}} - \frac{1}{2} \sigma_{ik}^{\text{aux}} \varepsilon_{ik}^{\text{aux}} \delta_{1j} \right\}_{,j} q \, dA, \tag{8}$$

and the resulting form of the interaction integral (M), based on the non-equilibrium formulation, is given by

$$M = \int_A \{ \sigma_{ij} u_{i,1}^{\text{aux}} + \sigma_{ij}^{\text{aux}} u_{i,1} - \sigma_{ik} \varepsilon_{ik}^{\text{aux}} \delta_{1j} \} q_{,j} \, dA + \int_A \{ \sigma_{ij} u_{i,1}^{\text{aux}} + \sigma_{ij}^{\text{aux}} u_{i,1} - \sigma_{ik} \varepsilon_{ik}^{\text{aux}} \delta_{1j} \}_{,j} q \, dA$$
$$= M_1 + M_2. \tag{9}$$

Moreover, the last term of the second integral (M_2) in Eq. (9) is expressed as

$$(\sigma_{ik} \varepsilon_{ik}^{\text{aux}} \delta_{1j})_{,j} = (\sigma_{ik} \varepsilon_{ik}^{\text{aux}})_{,1} = (\sigma_{ij} \varepsilon_{ij}^{\text{aux}})_{,1} = (C_{ijkl} \varepsilon_{kl} \varepsilon_{ij}^{\text{aux}})_{,1}$$
$$= C_{ijkl,1} \varepsilon_{kl} \varepsilon_{ij}^{\text{aux}} + \sigma_{ij}^{\text{aux}} \varepsilon_{ij,1} + \sigma_{ij} \varepsilon_{ij,1}^{\text{aux}}. \tag{10}$$

Substituting Eq. (10) into Eq. (9), and using compatibility (actual and auxiliary) and equilibrium (actual) (i.e. $\sigma_{ij,j} = 0$ with no body force), one obtains the resulting interaction integral (M) as

$$M = \int_A \left\{ \sigma_{ij} u_{i,1}^{\text{aux}} + \sigma_{ij}^{\text{aux}} u_{i,1} - \sigma_{ik} \varepsilon_{ik}^{\text{aux}} \delta_{1j} \right\} q_{,j} \, \mathrm{d}A$$
$$+ \int_A \left\{ \underline{\sigma_{ij,j}^{\text{aux}} u_{i,1}} - C_{ijkl,1} \varepsilon_{kl} \varepsilon_{ij}^{\text{aux}} \right\} q \, \mathrm{d}A, \tag{11}$$

where the underlined term is a non-equilibrium term, which appears due to non-equilibrium of the auxiliary stress fields, and must be considered to obtain converged solutions. The last term is due to material non-homogeneity and involves the material gradient. The derivatives of the auxiliary stress field in Eq. (2) are

$$\sigma_{ij,j}^{\text{aux}} = C_{ijkl,j}(\boldsymbol{x}) \, \varepsilon_{kl}^{\text{aux}} + C_{ijkl}(\boldsymbol{x}) \, \varepsilon_{kl,j}^{\text{aux}}$$
$$= \underline{(C_{ijkl})_{\text{tip}} \, \varepsilon_{kl,j}^{\text{aux}}} + C_{ijkl,j}(\boldsymbol{x}) \, \varepsilon_{kl}^{\text{aux}} + (C_{ijkl}(\boldsymbol{x}) - (C_{ijkl})_{\text{tip}}) \, \varepsilon_{kl,j}^{\text{aux}}, \tag{12}$$

where the underlined term in Eq. (12) vanishes.

The existence of the integral involving the non-equilibrium term as r goes to zero is proved below. The stiffness tensor involving material properties $E(r, \theta)$ and $v(r, \theta)$ must be continuous and differentiable function, and thus it can be written as (Eischen, 1987)

$$C_{ijkl}(r, \theta) = (C_{ijkl})_{tip} + r C_{ijkl}^{(1)}(\theta) + \frac{r^2}{2} C_{ijkl}^{(2)}(\theta) + O(r^3) + \cdots \tag{13}$$

where $C_{ijkl}^{(n)}(\theta)$ ($n = 1, 2, \ldots$) are angular functions. In Eq. (12), the first term vanishes because of equilibrium, and here we focus on the third term only. For the auxiliary fields for SIFs ($u_i^{\text{aux}}(\sqrt{r}, \theta)$, $\varepsilon_{ij}^{\text{aux}}(r^{-1/2}, \theta)$), the integral, as the limit r goes to zero, becomes

$$\lim_{A \to 0} \int_A \sigma_{ij,j}^{\text{aux}} \, u_{i,1} \, q \, \mathrm{d}A = \lim_{r \to 0} \int_\theta \int_r \sigma_{ij,j}^{\text{aux}} \, u_{i,1} \, q \, r \, \mathrm{d}r \, \mathrm{d}\theta$$

$$= \lim_{r \to 0} \int_\theta \int_r (C_{ijkl}(r, \theta) - (C_{ijkl})_{\text{ti}p}) \, \varepsilon_{kl,j}^{\text{aux}} \, u_{i,1} \, q \, r \, \mathrm{d}r \, \mathrm{d}\theta$$

$$= \lim_{r \to 0} \int_\theta \int_r O(r) \, O(r^{-3/2}) \, O(r^{-1/2}) \, q \, r \, \mathrm{d}r \, \mathrm{d}\theta$$

$$= \lim_{r \to 0} O(r) = 0. \tag{14}$$

Thus the limit exists and the proposed integral is well-posed.

3.3. EVALUATION OF STRESS INTENSITY FACTORS IN FGMs

The relationship between *J*-integral and the mode I and mode II SIFs is given as

$$J_{\text{local}} = \frac{K_{\text{I}}^2 + K_{\text{II}}^2}{E_{\text{tip}}^*} \tag{15}$$

where $E_{\text{tip}}^* = E_{\text{tip}}$ for plane stress and $E_{\text{tip}}/(1 - v_{\text{tip}}^2)$ for plane strain. For two admissible fields, which are the actual ($\boldsymbol{u}, \boldsymbol{\varepsilon}, \boldsymbol{\sigma}$) and auxiliary ($\boldsymbol{u}^{\text{aux}}, \boldsymbol{\varepsilon}^{\text{aux}}, \boldsymbol{\sigma}^{\text{aux}}$) fields, one obtains (Yau et al., 1980)

$$J_{\text{local}}^{s} = \frac{(K_{\text{I}} + K_{\text{I}}^{\text{aux}})^2 + (K_{\text{II}} + K_{\text{II}}^{\text{aux}})^2}{E_{\text{tip}}^*} \tag{16}$$

$$= J_{\text{local}} + J_{\text{local}}^{\text{aux}} + M_{\text{local}} \tag{17}$$

where J_{local} is given by Eq. (15), $J_{\text{local}}^{\text{aux}}$ is given by

$$J_{\text{local}}^{\text{aux}} = \frac{(K_{\text{I}}^{\text{aux}})^2 + (K_{\text{II}}^{\text{aux}})^2}{E_{\text{tip}}^*} \tag{18}$$

and M_{local} is given by

$$M_{\text{local}} = \frac{2}{E_{\text{tip}}^*}(K_{\text{I}} K_{\text{I}}^{\text{aux}} + K_{\text{II}} K_{\text{II}}^{\text{aux}}) \tag{19}$$

The mode I and mode II SIFs are decoupled and are evaluated as follows:

$$K_{\text{I}} = \frac{E_{\text{tip}}^*}{2} M_{\text{local}}^{(1)}, \quad (K_{\text{I}}^{\text{aux}} = 1.0, K_{\text{II}}^{\text{aux}} = 0.0) \tag{20}$$

$$K_{\text{II}} = \frac{E_{\text{tip}}^*}{2} M_{\text{local}}^{(2)}, \quad (K_{\text{I}}^{\text{aux}} = 0.0, K_{\text{II}}^{\text{aux}} = 1.0) \tag{21}$$

The relationships of Eqs. (20) and (21) are the same as those for homogeneous materials (Yau et al., 1980) except that, for FGMs, the material properties are evaluated at the crack-tip location (Dolbow and Gosz, 2002; Rao and Rahman, 2003; Kim and Paulino, 2003b).

4. A fracture criterion

Based on the concept of local homogenization (see Figure 2), fracture criteria originally developed for homogeneous materials can be extended to non-homogeneous materials such as FGMs (Konda and Erdogan, 1994; Gu and Asaro, 1997; Rousseau and Tippur, 2000; Kim and Paulino, 2003a; Kim, 2003). For instance, these criteria may include maximum hoop stress (Erdogan and Sih, 1963), maximum energy release rate (Hussain et al., 1974; Palaniswamy and Knauss, 1978), minimum strain energy density (Sih, 1974), $K_{\text{II}} = 0$ criterion (Cotterell and Rice, 1980), and criteria related to the minimum plastic zone radius (Golos and Wasiluk, 2000; Wasiluk and Golos, 2000; Khan and Khraisheh, 2004). As indicated in the introduction of this paper, the maximum energy release rate criterion is the method of choice in this work.

The maximum strain energy release rate, or $[\mathcal{G}(\theta)]_{\text{max}}$, criterion was proposed by Hussain et al. (1974) for homogeneous materials. They postulated that the crack subjected to combined loads will grow in the direction along which strain energy release is maximum and the crack will start to grow when the maximum strain energy release rate reaches a critical value. As mentioned in the introduction, here we consider a local (homogenized) version of the criterion by Hussain et al. (1974), which is appropriate for FGMs. The energy release rate for combined mode I and mode II loading in FGMs is given by

$$\mathcal{G} = \frac{K_{\text{I}}^2 + K_{\text{II}}^2}{E_{\text{tip}}^*}, \tag{22}$$

where $E_{\text{tip}}^* = E_{\text{tip}}$ for plane stress and $E_{\text{tip}}/(1 - v_{\text{tip}}^2)$ for plane strain. Eq. (22) is obtained by assuming that a crack under mixed-mode loading moves along its own plane. However, in general, the crack grows in a direction which is not parallel to its initial plane. Hussain et al. (1974) obtained an elasticity solution for a straight main crack and a branch crack extended at an arbitrary angle, and computed the energy release rate in the limit as the propagation branch vanishes. The energy release rate, based on the solution by Hussain et al. (1974), is given by

$$\mathscr{G}(\theta) = \frac{4}{E_{\text{tip}}^*} \left(\frac{1}{3 + \cos^2 \theta}\right)^2 \left(\frac{1 - \pi/\theta}{1 + \pi/\theta}\right)^{\theta/\pi}$$
$$\times [(1 + 3\cos^2 \theta)K_{\text{I}}^2 + 8\sin\theta\cos\theta K_{\text{I}}K_{\text{II}} + (9 - 5\cos^2 \theta)K_{\text{II}}^2]. \tag{23}$$

Then the crack initiation angle θ_0 is obtained from

$$\partial\mathscr{G}(\theta)/\partial\theta = 0 \ \Rightarrow \ \theta = \theta_0. \tag{24}$$

Once the crack initiation angle is determined, the crack initiation condition is given by

$$\mathscr{G}(\theta_0) = \mathscr{G}_{\text{cr}}(\boldsymbol{x}), \tag{25}$$

where $\mathscr{G}_{\text{cr}}(\boldsymbol{x})$ is the critical energy release rate, and is a function of spatial coordinates given by

$$\mathscr{G}_{\text{cr}}(\boldsymbol{x}) = \frac{K_{\text{Ic}}^2(\boldsymbol{x})}{E_{\text{tip}}^*}, \tag{26}$$

where $K_{\text{Ic}}(\boldsymbol{x})$ is the fracture toughness function for FGMs.

5. Numerical simulation of crack propagation in FGMs

Fracture analysis and crack propagation are conducted using the FEM code I-FRANC2D. The geometry is discretized with isoparametric graded elements (Kim and Paulino, 2002b). The specific elements used consist of singular quarter-point six-node triangles (T6qp) for crack-tip discretization, eight-node serendipity elements (Q8) for a circular region around crack-tip elements, and regular six-node triangles (T6) in a transition zone to Q8 elements at the outer region. For the calculation of SIFs by means of the interaction integral, we use the domain involving 12 sectors (S12) and four rings (R4) at each step of crack propagation (see Figure 8(e)). Quasi-static automatic crack propagation in FGMs are performed in the following examples:
(1) A crack in a beam subjected to four-point bending.
(2) A crack in a beam subjected to three-point bending.
(3) A crack in a beam with holes subjected to three-point bending.
(4) A crack in a double cantilever beam under non-proportional loading.
   In order to validate the numerical results against available experimental results, we adopt the experimental data reported by Rousseau and Tippur (2000). The first example involves mixed-mode crack propagation in a graded glass/epoxy beam under four-point loading. The second example is based on the experimental and numerical investigation on a homogeneous poly-methyl-methacrylate (PMMA) three-point bending beam performed by Galvez et al. (1996), and it is extended to a graded beam. The third example investigates a crack in a PMMA beam with three holes under three-point bending, and it is extended to a graded material system. The last example is based on PMMA double cantilever beam subjected to non-proportional loading

performed by Galvez et al. (1996), and it is also extended to a graded specimen. For the last three examples, we have adopted material variations for the FGM specimen which are similar to those obtained in the experiments by Rousseau and Tippur (2000).

5.1.   A crack in a beam subjected to four-point bending

Rousseau and Tippur (2000) investigated crack growth behavior of a crack normal to the material gradient in a graded glass/epoxy subjected to four-point bending, and applied displacement controlled loading at a cross-head speed of 0.25 mm/min using the Instron Universal Testing Machine. The FGM beam was made of solid A-glass spheres of mean diameter 42 μm dispersed within a slow curing epoxy matrix, and was fabricated by gravity assisted casting technique with two-part slow curing epoxy and uncoated solid glass sphere fillers.

Figure 12(a) shows specimen geometry and boundary conditions (BCs) for a crack located at $\xi = 0.17$ (ξ is a normalized length variable), Figure 12(b) shows the complete mesh configuration, and Figure 12(c) shows mesh detail using 12 sectors (S12) and 4 rings (R4) around the crack tip. The typical mesh discretization consists of 1067 Q8, 155 T6, and 12 T6qp elements, with a total of 1234 elements and 3725 nodes. The following data are used for the FEM analyses:

$$\text{plane stress, } 2 \times 2 \text{ Gauss quadrature,}$$
$$a/W = 0.25, \quad t = 6 \text{ mm}, \quad P = P_{\text{cr}}(a + n\Delta a, X), \tag{27}$$

where n refers to the number of crack propagation increments, and $X = (X_1, X_2)$.

Figure 13 illustrates variations of Young's modulus E and Poisson's ratio v, and Figure 14 illustrates the variation of fracture toughness K_{Ic} in the graded material region. The numerical values of material properties at interior points in the graded region are illustrated in Table 1.

Figure 15 shows comparison of crack trajectories and crack initiation angles (θ_0) between the experimental results reported by Rousseau and Tippur (2000) and the present FEM results. The numerical results are obtained by considering the crack increment $\Delta a = 1$ mm (constant). There is good agreement in crack initiation angles and crack trajectories between numerical and experimental results.

Due to the lack of information on the critical load P_{cr} and load history in the paper by Rousseau and Tippur (2000), here we calculated the critical load at each step based on a specific fracture criterion, i.e., maximum energy release rate, and applied the calculated critical load to the corresponding step. Notice that there is no effect of the load magnitude on the crack trajectory within the framework of linear elastic analysis. Table 2 shows critical load P_{cr}, SIFs, and the phase angle ($\psi = \tan^{-1}(K_{\text{II}}/K_{\text{I}})$) at the initial step. Because $K_{\text{II}} < 0$, the crack initiation angle is counter-clockwise with respect to the local coordinate x_1 (see Figure 15).

Figure 16(a)–(e) shows finite element discretization and remeshing for initial, intermediate, and final steps of crack propagation considering the crack located at $\xi = 0.17$ and $\Delta a = 1$ mm. One can observe that local mesh refinement is done around the crack tip at each step. Figure 16(f) shows the fixed crack-tip template (S12,R4) used in every step of crack propagation.

To investigate the effect of the crack increment Δa on crack trajectory, Figure 17 shows comparison of crack trajectories obtained by considering $\Delta a = 0.5$, 1.0, and 2.0 mm. There is not much difference in the crack trajectory for the crack increments Δa considered here. However, inappropriate large values of the crack increment may lead to accumulative deviation of crack trajectory.
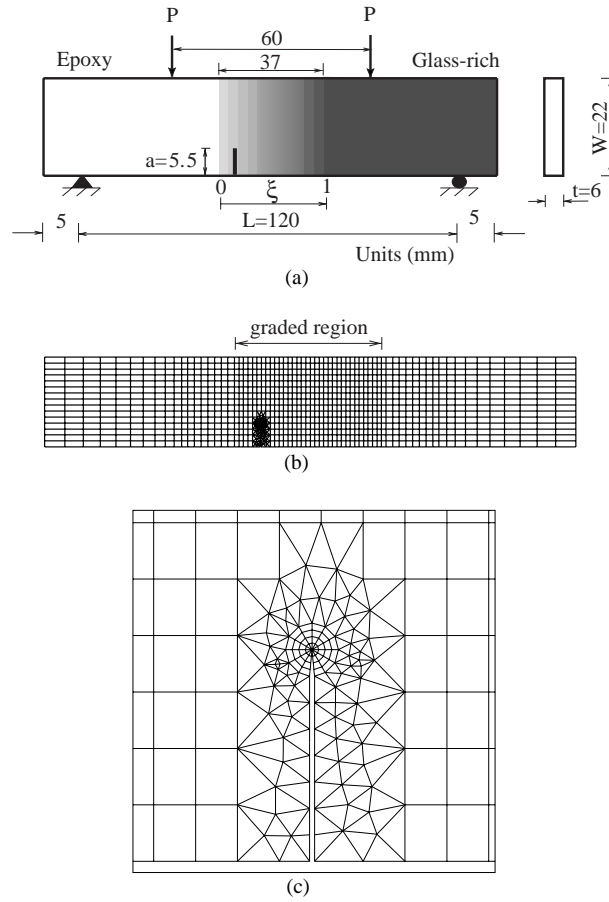
Figure 12. Example 1: A crack in a graded epoxy/glass beam subjected to four-point bending: (a) geometry and boundary conditions for a crack located at $\xi = 0.17$ (6.29 mm); (b) the complete mesh configuration; (c) mesh detail using 12 sectors (S12) and 4 rings (R4) around the crack tip.
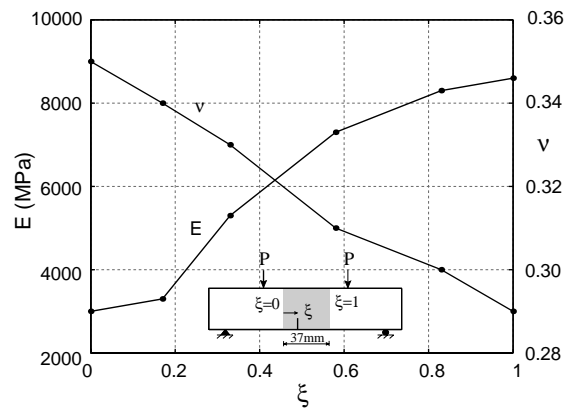

Figure 13. Example 1: Variations of Young's modulus E (MPa) and Poisson's ratio v along the graded region ($0 \leq \xi \leq 1$).
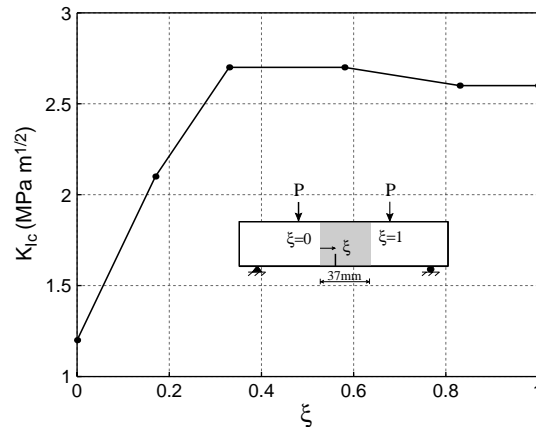
Figure 14. Example 1: Variation of fracture toughness K_{Ic} (MPa$\sqrt{m}$) along the graded region ($0 \leq \xi \leq 1$).

5.2. A CRACK IN A BEAM SUBJECTED TO THREE-POINT BENDING

Galvez et al. (1996) investigated crack growth behavior of a crack in a homogeneous PMMA beam subjected to three-point bending considering three different loading controls such as crack tip opening displacement (CMOD), displacement, and load (P). The material properties of the PMMA beam used are as follows:

$$E = 2890 \text{ MPa}, \ v = 0.4, \ K_{Ic} = 1.09 \text{ MPa}\sqrt{m}. \tag{28}$$

In this example, we consider both homogeneous and graded (along the X_2 direction) beams. Figure 18(a) and (b) shows the specimen geometry and BCs for two different boundary conditions: Cases 1 and 2, respectively; Figure 18(c) shows the complete mesh configuration; and Fig. 18(d) shows mesh detail using 12 sectors (S12) and 4 rings (R4) around the crack tip. Notice that the mesh of Figure 18(c) is valid for both cases, but the boundary conditions change.
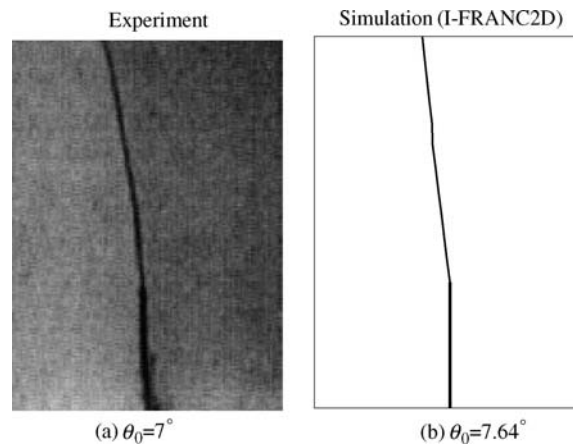
Figure 15. Example 1: Comparison of crack trajectories and crack initiation angles (θ_0) obtained (a) experimentally by Rousseau and Tippur (2000) who considered the crack located at $\xi = 0.17$ in an FGM beam with (b) the present FEM simulation using the maximum energy release rate criterion ($\Delta a = 1$ mm).

Table 2. Example 1: Numerical results for the critical load P_{cr}, SIFs, and phase angle ($\psi = \tan^{-1}(K_{II}/K_I)$) at the initial step

ξ	P_{cr} (N)	K_I (MPa$\sqrt{m}$)	K_{II} (MPa$\sqrt{m}$)	$\psi = \tan^{-1}(K_{II}/K_I)$
0.17	253.3	2.122	−0.129	−3.484

(a) Initial step

(b) Step 3

(c) Step 9

(d) Step 12

(e) Step 16 (final)

(f) Crack-tip template (shaded)
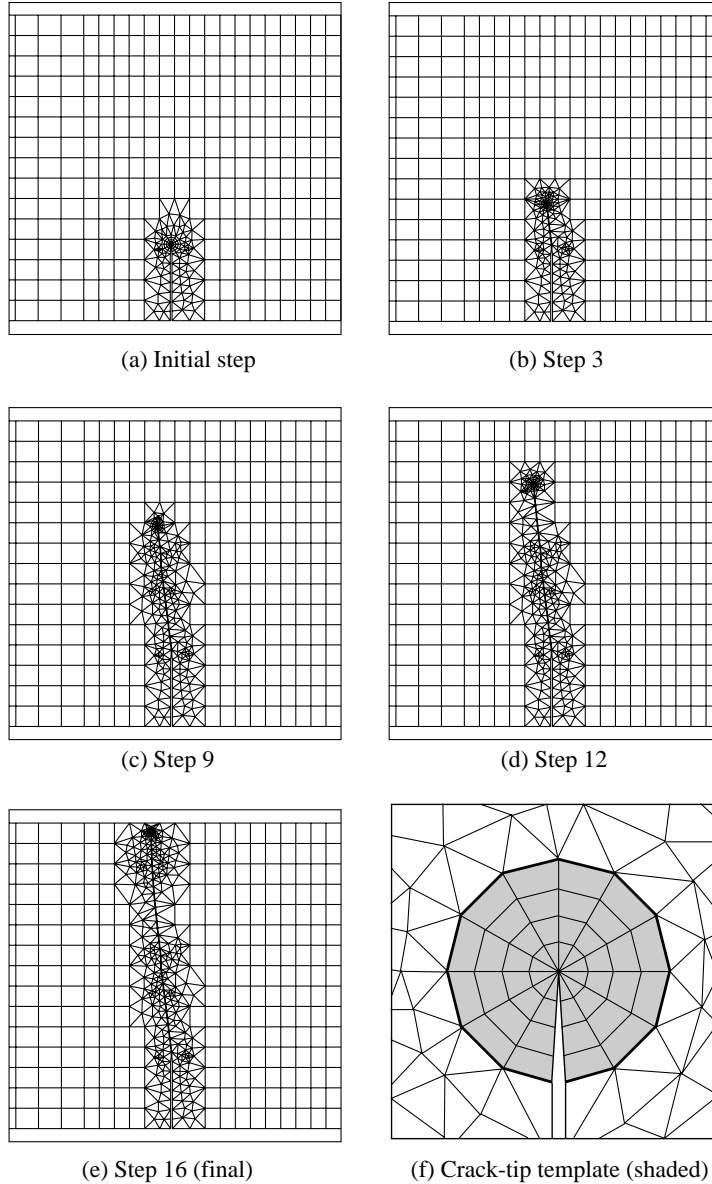
Figure 16. Example 1: finite element discretization and remeshing on each step of crack propagation considering $\xi = 0.17$ and $\Delta a = 1$ mm: (a) Initial step (Step 0); (b) Step 3; (c) Step 9; (d) Step 12; (e) final step (Step 16); (f) fixed crack-tip template (S12, R4) used in every step of crack propagation.
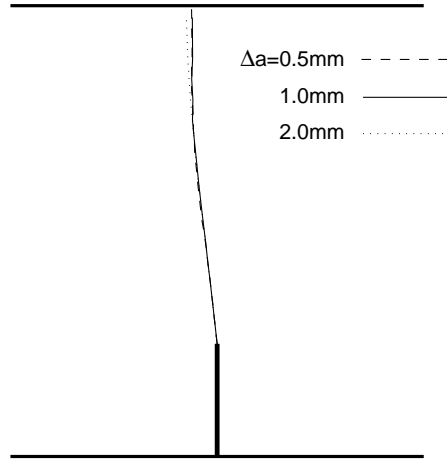
Figure 17. Example 1: Sensitivity of the crack trajectory with respect to the crack increment Δa, and comparison of solutions obtained with $\Delta a = 0.5$, 1.0, and 2.0 mm.

The mesh discretization consists of 741 Q8, 239 T6, and 12 T6qp elements, with a total of 992 elements and 2875 nodes. The following data are used for the FEM analyses:

$$\text{plane stress, } 2 \times 2 \text{ Gauss quadrature,}$$
$$a/W = 0.4, \; t = 18 \, \text{mm}, P = P_{\text{cr}}(a + n\Delta a, X). \tag{29}$$

For the homogeneous beam, we use the material properties of PMMA given by expressions (28). For the graded beam, we assumed linear variation of Young's modulus, Poisson's ratio, and fracture toughness, and these properties at the end points are given in Table 3. Figure 19 shows comparison of crack trajectories for a homogeneous PMMA beam obtained by the present numerical simulation with experimental (averaging) results reported by Galvez et al. (1996) for the *Case 2*. The numerical results are obtained by considering $\Delta a = 1.5$ mm (constant) and twenty-two steps including the initial step. There is reasonably good agreement between numerical and experimental results. Figure 20 shows comparison of crack trajectories for a homogeneous PMMA beam with those for a graded beam obtained by the present numerical simulation for the *Case 2* considering $\Delta a = 1.5$ mm and twenty-two steps including the initial step. Notice that, in this case, the material gradation has almost no effect in the crack trajectory.

Figure 21 shows comparison of load versus crack mouth opening displacement (CMOD) curve for a homogeneous beam with that for a graded beam obtained by the present numerical simulation for *Case 1* (mode I cracking) considering $\Delta a = 1.5$ mm. As expected, the linear relationship between load and CMOD is observed up to the initial step. Notice that the critical load (P_{cr}) and corresponding CMOD at the initial step for the FGM are greater than those for the homogeneous beam. This indicates that the crack initiation is delayed due to material gradation.

Figure 22 shows comparison of load versus CMOD curve for a homogeneous beam with that for a graded beam obtained by the present numerical simulation for Case 2 (mixed-mode cracking), which also considers $\Delta a = 1.5$ mm. Notice that the critical load (P_{cr}) and corresponding CMOD for the FGM at the initial step are also greater than those for the
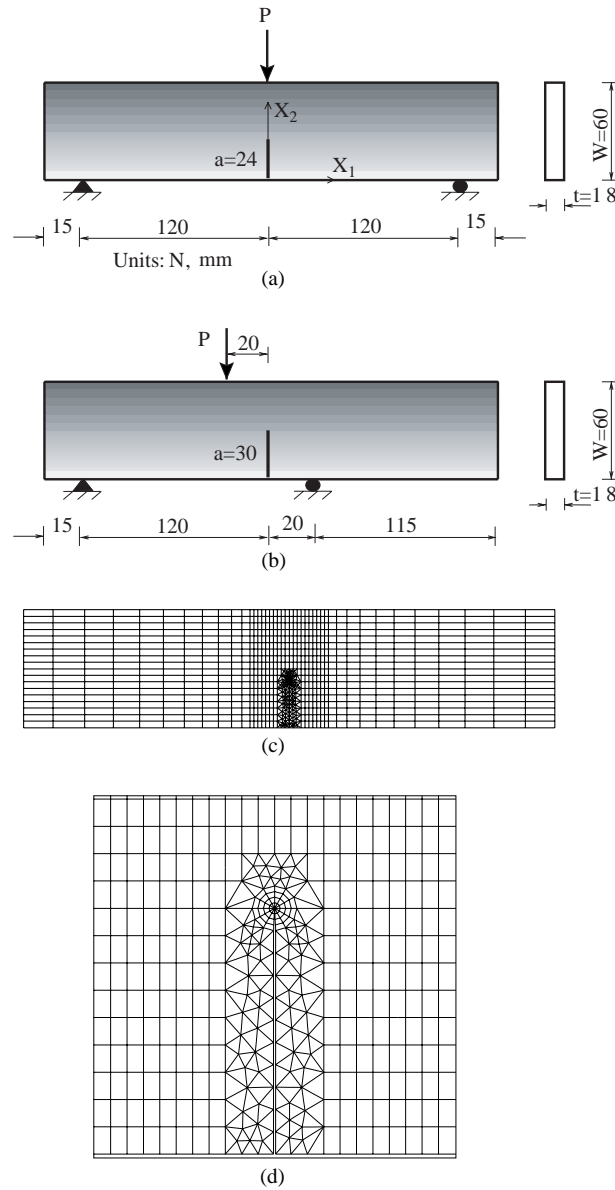
Figure 18. Example 2: A crack in a beam subjected to three-point bending (Units: N, mm): (a) *Case 1*: geometry and boundary conditions considering symmetric loading; (b) *Case 2*: geometry and boundary conditions considering offset loading; (c) the complete mesh configuration; (d) mesh detail using 12 sectors (S12) and 4 rings (R4) around the crack-tip.

homogeneous beam. By comparing Figures 21 and 22, one can observe that, for both homogeneous and graded beams, the critical load (P_{cr}) for *Case 2* is over twice as much as that for *Case 1*.

Figure 23(a) shows finite element discretization and remeshing for the final step of crack propagation considering $\Delta a = 1.5$ mm for both homogeneous and graded beams of *Case 1*. Notice that the crack grows vertically because of symmetry. Figure 23(b) shows finite element discretization and remeshing for the final step of crack propagation considering $\Delta a = 1.5$ mm

Table 3. Example 2: Material properties (Young's modulus E, Poisson's ratio v, and fracture toughness K_{Ic}) at the end points in the graded region. The material gradation varies linearly in between the end points. The material properties at the middle point ($X_2 = 30$ mm) are the same as those for the homogeneous PMMA beam

X_2 (mm)	E (MPa)	v	K_{Ic} (MPa$\sqrt{m}$)
0	1780	0.41	0.99
60	4000	0.39	1.19

for the homogeneous beam of *Case 2*. The final mesh for the FGM beam is almost identical to the Figure 23(b).

5.3. A crack in a beam with holes subjected to three-point bending

Bittencourt et al. (1996) provided experimental and numerical results for a crack in a homogeneous PMMA beam with three holes subjected to three-point bending. Here material properties for the homogeneous beam are as follows:

$$E = 1, \quad v = 0.3, \quad K_{Ic} = 1, \tag{30}$$

where E and K_{Ic} are normalized quantities. The actual material properties are not available in the reference by Bittencourt et al. (1996).

In this example we consider both homogeneous and graded beams. Figure 24(a) and (b) shows specimen geometry and BCs, and the complete mesh configuration, respectively, and Fig. 24(c) shows mesh detail using 12 sectors (S12) and 4 rings (R4) around the crack tip.

The mesh discretization consists of 680 Q8, 145 T6, and 12 T6qp elements, with a total of 837 elements and 2490 nodes. The following data are used for the FEM analyses:
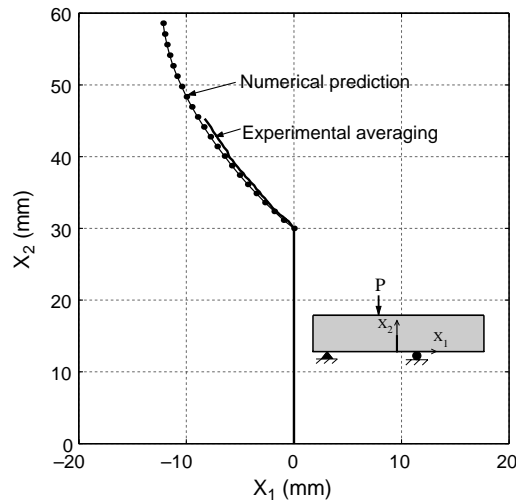
Figure 19. Example 2, Case 2: comparison of crack trajectories for homogeneous PMMA beam obtained by the present numerical simulation with experimental (averaging) results reported by Galvez et al. (1996). The numerical results are obtained considering $\Delta a = 1.5$ mm (constant).
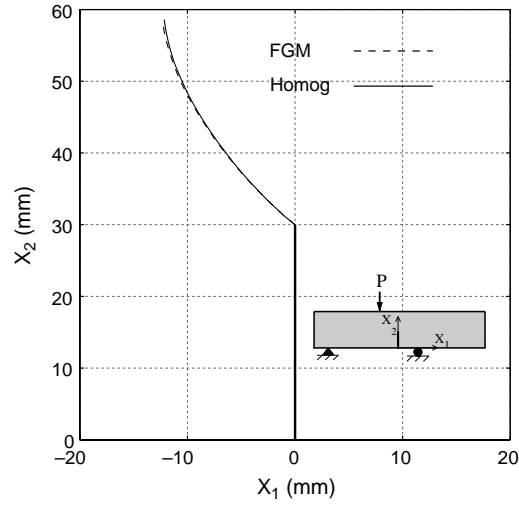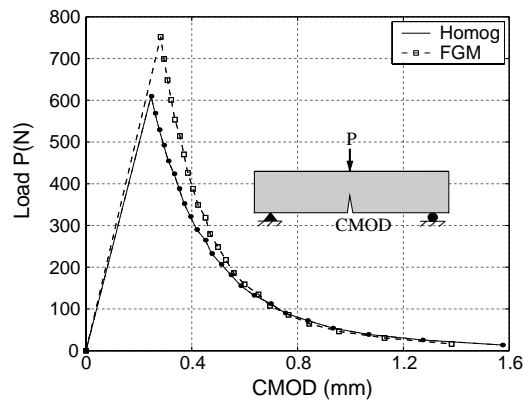
Figure 20. Example 2, Case 2: comparison of crack trajectories for a homogeneous beam with those for a graded beam obtained by the present numerical simulation. The numerical results are obtained considering $\Delta a = 1.5$ mm (constant).

plane stress, 2×2 Gauss quadrature,

$$a/W = 0.1875, \quad t = 25.4 \, \text{mm} \ (1 \, \text{in.}), \quad P = 4.45 \, \text{N} (1 \, \text{lb.}).$$ (31)

For the homogeneous beam, we use the material properties of PMMA given by the expressions in (30). For the graded beam, we consider three regions, and in the middle region assume linear variation of Young's modulus, Poisson's ratio, and fracture toughness, as shown in Figs. 25 and 26, respectively. Figure 27(a) shows comparison of crack trajectories obtained by the present numerical results with experimental results reported by Bittencourt et al. (1996) for the homogeneous beam. The numerical results are obtained by considering $\Delta a = 7.62$ mm (0.3 in.), as adopted by Bittencourt et al. (1996), and 12 steps. There is excellent agreement between numerical and experimental results. Figure 27(b) shows comparison of crack trajectories

Figure 21. Example 2, Case 1: comparison of P-CMOD curve for a homogeneous beam with that for a graded beam obtained by the present numerical simulation. The numerical results are obtained considering $\Delta a = 1.5$ mm (constant).
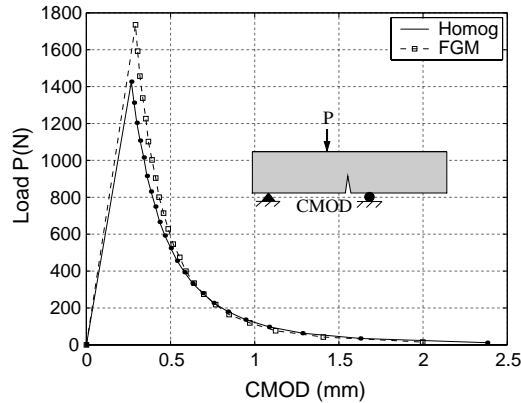
Figure 22. Example 2, Case 2: comparison of P-CMOD curve for a homogeneous beam with that for a graded beam obtained by the present numerical simulation. The numerical results are obtained considering $\Delta a = 1.5$ mm (constant).

obtained by the present numerical results for the graded beam with those for the homogeneous beam. The numerical results are obtained by considering $\Delta a = 7.62$ mm and 11 steps. As one would expect, there is significant difference in crack trajectories. Note that, for the FGM beam, Young's modulus on the left-hand side is less than that on the right-hand side. Thus the crack growth direction is naturally inclined to the left. Figure 28(a) and (b) shows finite element discretization and remeshing for the final step of crack propagation considering $\Delta a = 7.62$ mm for both homogeneous and graded beams, respectively. Figure 28(c) and (d) shows the contour plots for the maximum principal stress for the homogeneous and graded beams.

Figure 29 shows SIFs history for both homogeneous and graded beams with respect to crack extension ($\Delta a = 7.62$ mm). There is a monotonic increasing behavior of mode I SIF (K_{I}) for the FGM beam, however, this behavior is not observed for the homogeneous beam, which shows decreasing SIFs from steps 5 and 6. For the homogeneous beam, this behavior is due to the hole adjacent to the crack. For both homogeneous and graded beams, the mode II SIF K_{II} oscillates around zero thus changing the sign of the crack initiation angles.
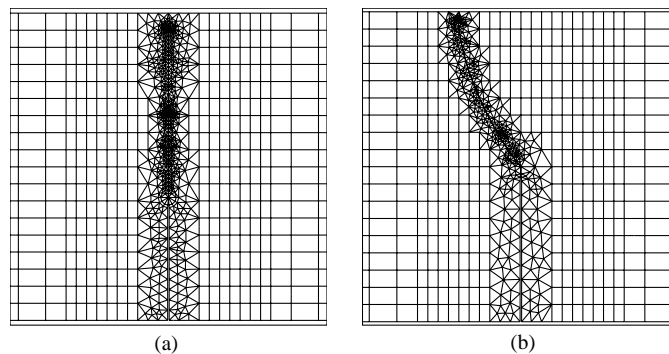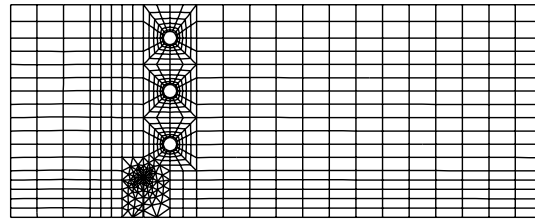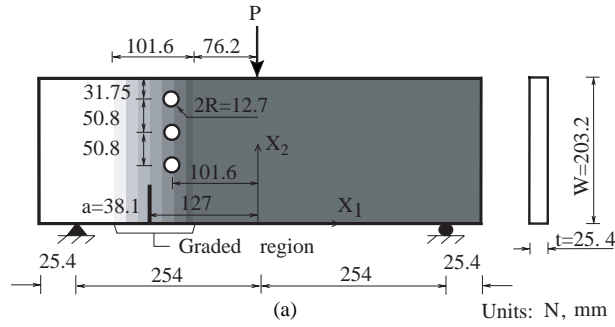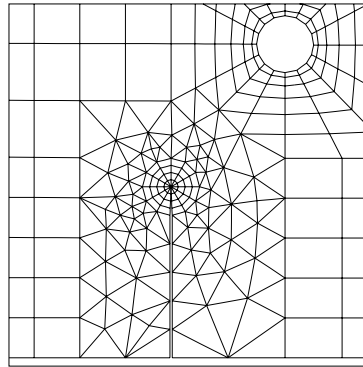

Figure 23. Example 2: finite element discretization and remeshing considering $\Delta a = 1.5$ mm: (a) Case 1: homogeneous and FGM beams; (b) Case 2: homogeneous beam; it is interesting to observe that, in this case, the final mesh for the FGM beam is almost identical to this one (cf. Figure 20).

Figure 24. Example 3: A crack in a beam with three holes subjected to three-point bending (Units: N, mm): (a) geometry and boundary conditions; (b) the complete mesh configuration; (c) mesh detail using 12 sectors (S12) and 4 rings (R4) around the crack tip.

5.4. A CRACK IN A DOUBLE CANTILEVER BEAM UNDER NON-PROPORTIONAL LOADING

This example investigates crack propagation considering non-proportional loading. The external loading at the crack propagation step t can be written as

$$P_i(t) = \alpha_i(t)P_i^0, \quad i = 1, \ldots, n \tag{32}$$

where i represents n different loads, P_i^0 is a constant for the ith load, and $P_i(t)$ is the ith load applied at the crack propagation step t. In this paper, the definitions of proportional and non-proportional loadings are made comparing the ratio of the loads between the initial step t_1 and the step t_m ($m = 2, \ldots, s$ where s is the number of steps considered) for both the ith and the jth loads. For instance, let's consider two loadings, i.e. $P_1(t)$ and $P_2(t)$. If
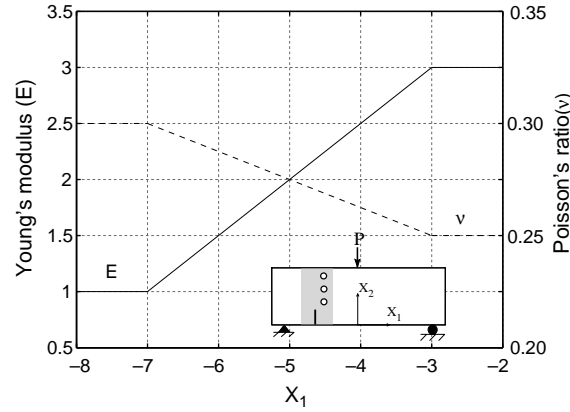
Figure 25. Example 3: Variations of Young's modulus E (normalized) and Poisson's ratio v in the three regions.

$$\frac{\alpha_1(t_m)}{\alpha_1(t_1)} \neq \frac{\alpha_2(t_m)}{\alpha_2(t_1)}, \quad \text{for } m = 2, \ldots, s \tag{33}$$

then the loads $P_1(t)$ and $P_2(t)$ are non-proportional to each other. On the other hand, if

$$\frac{\alpha_1(t_m)}{\alpha_1(t_1)} = \frac{\alpha_2(t_m)}{\alpha_2(t_1)}, \quad \text{for } m = 2, \ldots, s \tag{34}$$

then the loads $P_1(t)$ and $P_2(t)$ are proportional to each other.

To show the procedure for searching the critical load, let's consider a fracture envelope for a crack subjected to two independent loadings: varying load P_1 and constant load P_2 as shown in Figure 30. The mixed-mode SIFs are denoted by K_I^i and K_{II}^i for the corresponding load P_i ($i = 1, 2$). Superposition of the two fields $P = P_1 + P_2$ leads to SIFs located at the point A inside a fracture envelope. To achieve critical SIFs at the point B for crack growth, one needs to increase P_1, for instance P_1 to $P_{cr} = P_1 + \Delta P_1$, which results in the increase of the SIFs by
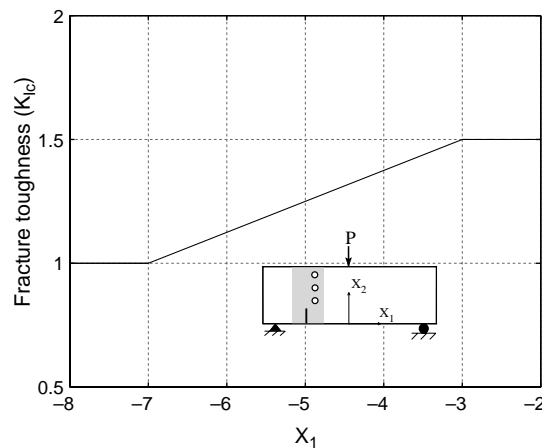

Figure 26. Example 3: Variations of fracture toughness K_{Ic} (normalized) in the three regions.
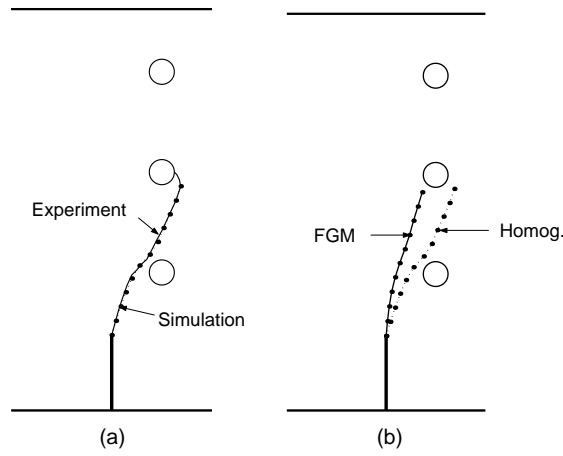
Figure 27. Example 3: Comparison of crack trajectories: (a) the present numerical results (dotted line) for the homogeneous beam versus experimental results (solid line) reported by Bittencourt et al. (1996). (b) the present numerical results for the graded beam (solid line) versus those for the homogeneous beam. The numerical results are obtained by considering $\Delta a = 7.62$ mm.
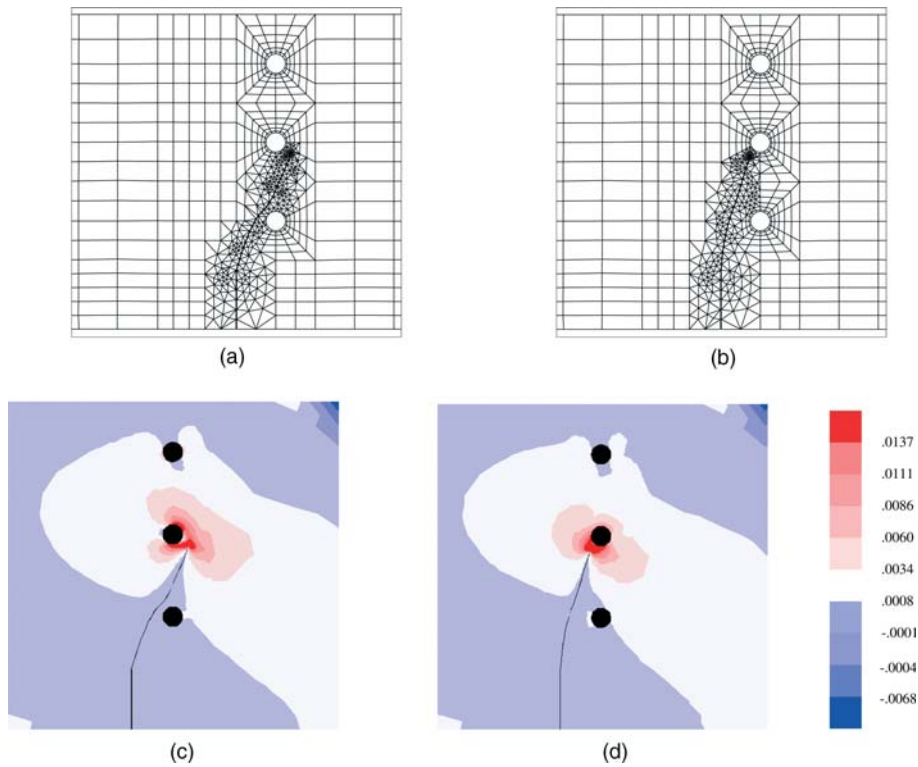

Figure 28. Example 3: finite element remeshing considering $\Delta a = 7.62$ mm, and the contour plots of the maximum principal stress (MPa): (a) homogeneous beam; (b) graded beam. The color scale for stress ranges from -0.0068 MPa $(-1.0$ psi) to 0.01378 MPa (2.0 psi).
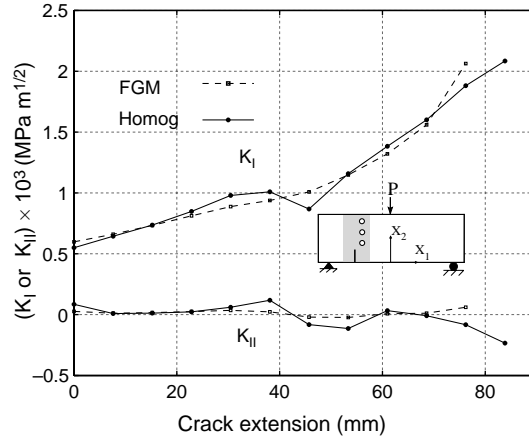
Figure 29. Example 3: History of mixed-mode SIFs (K_I or K_{II}) $\times 10^3$ MPa$\sqrt{m}$ with respect to crack extension ($\Delta a = 7.62$ mm). The twelve and eleven steps are performed for the homogeneous and graded beams, respectively.

$(K_{II}^1/K_I^1) \times \Delta P_1$. This scheme is used to search for the critical load P_{cr} and its corresponding SIFs for non-proportional loading at each step of crack propagation.

Galvez et al. (1996) performed experimental and numerical investigations on crack growth behavior of a crack in a double cantilever PMMA beam subjected to non-proportional loading. The material properties of the PMMA beam used are the same as those for the second example, and are given in Eq. (28). In this example, we consider both homogeneous and graded beams. Figure 31(a) shows specimen geometry and BCs, Figure 31(b) shows the complete mesh configuration, and Figure 31(c) shows mesh detail using 12 sectors (S12) and 4 rings (R4) around the crack tip. In the context of previous discussion (see Figure 30), P is variable (analogous to P_1) and Q is constant (analogous to P_2).

The mesh discretization consists of 2101 Q8, 286 T6, and 12 T6qp elements, with a total of 2399 elements and 6970 nodes. The following data are used for the FEM analyses:

$$\text{plane stress}, 2 \times 2 \text{ Gauss quadrature},$$
$$a = 30 \text{ mm}, \quad t = 18 \text{ mm}, \quad P = P_{cr}(a + n\Delta a, X), Q = 79.4 \text{ N (constant)}. \tag{35}$$
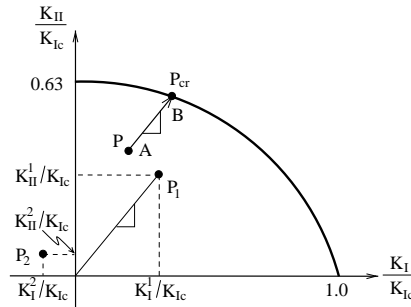

Figure 30. Example 4: procedure for crack initiation in a fracture envelope based on maximum energy release rate criterion considering *non-proportional loading*.
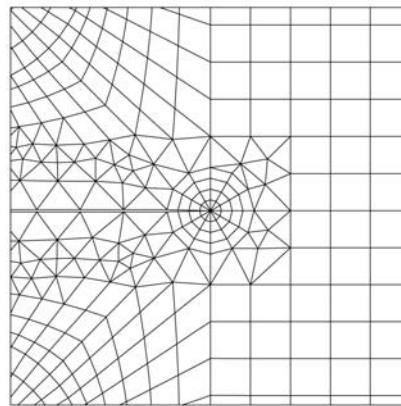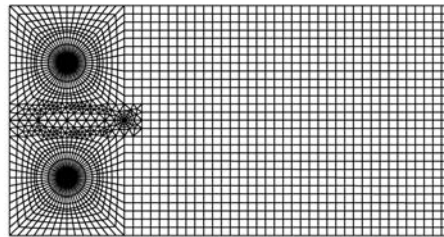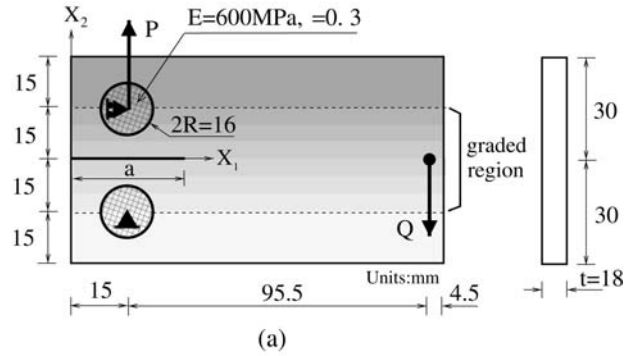
Figure 31. Example 4: A crack in a double cantilever beam: (a) geometry and boundary conditions; (b) the complete mesh configuration; (c) mesh detail using 12 sectors (S12) and four rings (R4) around the crack-tip.

For the homogeneous beam, we use the material properties of PMMA given by Eq. (28). For the graded beam, we adopted variation of material properties from the first example considering the graded region -15 mm $\leq X_2 \leq 15$ mm, which corresponds to $0 \leq \xi \leq 0.81$ (cf. Figures 13 and 14) in the first example. Here we assume two cases (*Cases 1* and *2*) of material variation as shown in Figure 32 (cf. Figure 12(a)).

Figure 33 shows comparison of crack trajectories for homogeneous PMMA double cantilever beam obtained by the present numerical simulation with those for both CMOD-controlled and displacement-controlled experiments performed by Galvez et al. (1996). For the present
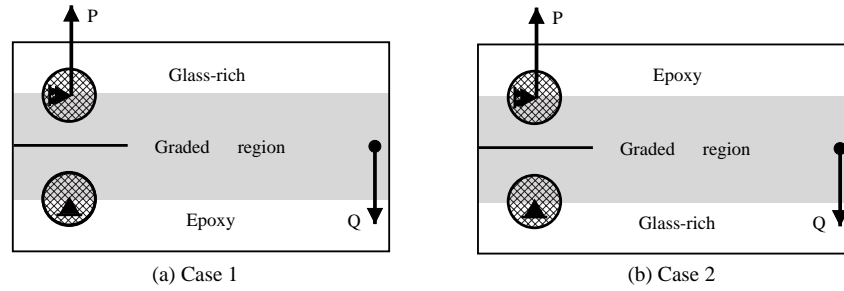
(a) Case 1   (b) Case 2

Figure 32. Example 4: two cases of FGM double cantilever beams: (a) Case 1; (b) Case 2. The variations of material properties are adopted from the first example considering the material gradation in the X_2 direction along the region -15 mm $\leq X_2 \leq 15$ mm (cf. Figures 13 and 14).

simulation and the displacement-controlled experiment (Galvez et al., 1996), the load $Q = 79.4$ N is used, however, the load $Q = 79.9$ N is used for CMOD-controlled loading (Galvez et al., 1996). The present simulation result is similar to the CMOD-controlled experiment result. Figure 34 shows comparison of crack trajectories for homogeneous PMMA double cantilever beam obtained by the present numerical simulation with those for the FGM beams (Cases 1 and 2). The variation of Young's modulus shows much influence on crack trajectories. For Case 1, the crack grows to the weaker part of the material, and for Case 2, the crack deflects towards the left side of the crack trajectory for the homogeneous case due to the influence of the material variation. Figure 35 compares load versus CMOD curve for a homogeneous double cantilever beam obtained by the present numerical simulation with that for the FGM cases (Cases 1 and 2) considering $\Delta a = 2.0$ mm. As expected, the linear relationship between load and CMOD is observed up to the initial step. Notice that, for the homogeneous case, as the crack grows by Δa, the load P_{cr} decreases and its corresponding CMOD generally shows an increasing behavior; however, for the FGM case, this behavior of CMOD is not observed for steps 9–13 in the FGM Case 1 and for steps 8–11 in the FGM Case 2 (see Figure 35). This is due to the steep gradient of fracture toughness in the graded region (see Figures 14 and 34). Due to higher fracture
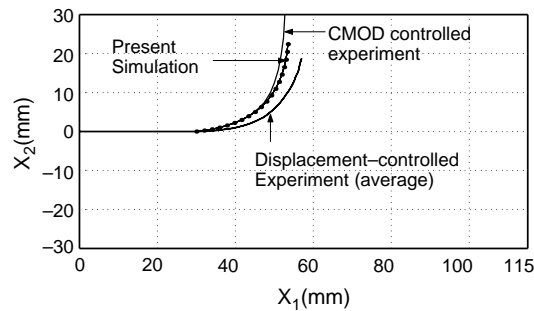

Figure 33. Example 4: comparison of crack trajectories for homogeneous PMMA double cantilever beam obtained by the present numerical simulation with those for CMOD-controlled and displacement-controlled experiments performed by Galvez et al. (1996). For the present simulation and the displacement-controlled experiment, the load $Q = 79.4$ N is used, however, the load $Q = 79.9$ N is used for CMOD-controlled loading. The numerical results are obtained by considering $\Delta a = 2.0$ mm.
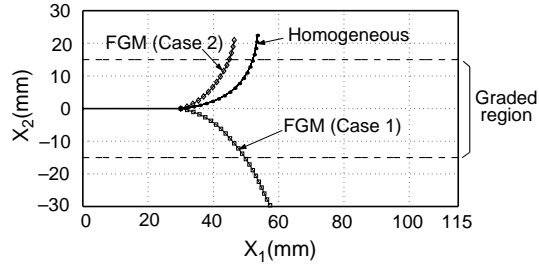
Figure 34. Example 4: comparison of crack trajectories for homogeneous PMMA double cantilever beam obtained by the present numerical simulation with those for the FGM beams (Cases 1 and 2). The numerical results are obtained by considering $\Delta a = 2.0$ mm.

Figure 35. Example 4: comparison of load versus CMOD curve for a homogeneous double cantilever beam obtained by the present numerical simulation with those for the FGM beams (Cases 1 and 2). The numerical results are obtained by considering $\Delta a = 2.0$ mm and $Q = 79.4$ N.
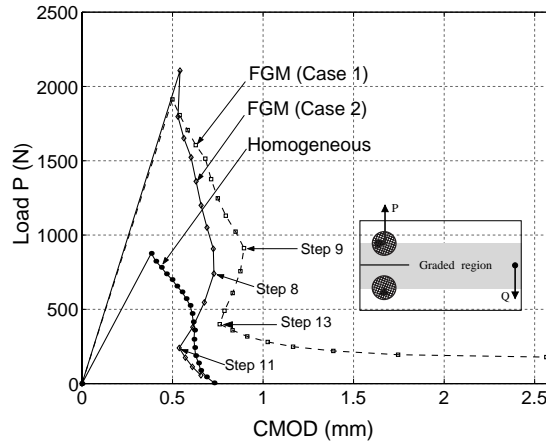
toughness in the FGM beams, the critical load P_{cr} at the initial step for the FGM beams is increased, and thus crack initiation is delayed.

6. Concluding remarks and extensions

This paper investigates fracture behavior of FGMs by performing automatic simulation of crack propagation by means of a remeshing scheme in conjunction with the finite element method. This paper focuses on accurate evaluation of mixed-mode SIFs in FGMs using the interaction integral method tailored for FGMs and subsequent prediction of crack trajectory. The crack propagation is performed under mixed-mode loading conditions (naturally induced by material non-homogeneity) and also under non-proportional loading.

Based on local homogenization, we use the maximum energy release rate criterion (Hussain et al., 1974). Crack trajectories obtained by this fracture criterion agree well with available experimental results for homogeneous and FGMs. Moreover, we observe that history of SIFs and critical loads for FGMs is significantly different from that for a homogeneous material. The

present approach requires a user-defined crack increment at the beginning of simulation. In the first example of this paper, a brief convergence study was presented to investigate the sensitivity of the crack trajectory with respect to the crack increment. For homogeneous materials, Hori and Vaikuntan (1997) proposed a formulation to determine the curvature and length of a small crack extension. Thorough investigation on crack increment in FGMs is needed in conjunction with experiments. The computational scheme developed here serves as a guideline for fracture experiments on homogeneous and FGM specimens (e.g. initiation toughness and *R*-curve).

Potential extension of the present work consists of investigating the effect of T-stress (non-singular stress) on crack initiation angles in brittle FGMs (Kim and Paulino, 2003a) and assessing various fracture criteria for crack propagation in FGMs. Another potential extension involves developing nonlinear material models for FGMs, evaluating fracture parameter (*J*-integral), and simulating crack propagation in elastic-plastic FGMs.

References

Abanto-Bueno, J. and Lambros, J. (2002). Investigation of crack growth in functionally graded materials using digital image correlation.*Engineering Fracture Mechanics* **69**(14–16), 1695–1711.

Becker, T.L. Jr., Cannon, R.M. and Ritchie, R.O. (2001). Finite crack kinking and T-stresses in functionally graded materials. *International Journal of Solids and Structures* **38**(32–33), 5545–5563.

Bittencourt, T.N., Wawrzynek, P.A. and Ingraffea, A.R. (1996). Quasi-static simulation of crack propagation for 2D LEFM problems. *Engineering Fracture Mechanics* **55**(2), 321–334.

Budiansky, B. and Rice, J.R. (1973). Conservation laws and energy-release rates. *Journal of Applied Mechanics, Transactions ASME* **40**(1), 201–203.

Carpenter, R.D., Liang, W.W., Paulino, G.H., Gibeling, J.C. and Munir, Z.A. (1999). Fracture testing and analysis of a layered functionally graded Ti/TiB beam in 3-point bending. *Materials Science Forum* **308**, 837–842.

Chang, J.H. and Chien, A.J. (2002). Evaluation of M-integral for anisotropic elastic media with multiple defects. *International Journal of Fracture* **114**(3), 267–289.

Cotterell, B. and Rice, J.R. (1980). Slightly curved or kinked cracks. *International Journal of Fracture* **16**(2), 155–169.

Dolbow, J. and Gosz, M. (2002). On the computation of mixed-mode stress intensity factors in functionally graded materials. *International Journal of Solids and Structures* **39**(9), 2557–2574.

Eftis, J., Subramonian, N. and Liebowitz, H. (1977). Crack border stress and displacement equations revisited. *Engineering Fracture Mechanics* **9**(1), 189–210.

Eischen, J.W. (1987). Fracture of non-homogeneous materials. *International Journal of Fracture* **34**(1), 3–22.

Erdogan, F. (1995). Fracture mechanics of functionally graded materials. *Composites Engineering* **5**(7), 753–770.

Erdogan, F. and Sih, G.C. (1963). On the crack extension in plates under plane loading and transverse shear. *ASME Journal of Basic Engineering* **85**(4), 519–527.

Galvez, J., Elices, M., Guinea, G.V. and Planas, J. (1996). Crack trajectories under mixed mode and non-proportional loading. *International Journal of Fracture* **81**(2), 171–193.

Golos, K. and Wasiluk, B. (2000). Role of plastic zone in crack growth direction criterion under mixed mode loading. *International Journal of Fracture* **102**(4), 341–353.

Gu, P. and Asaro, R.J. (1997). Crack deflection in functionally graded materials. *International Journal of Solids and Structures* **34**(24), 3085–3098.

Hirai, T. (1993). Functionally gradient materials and nanocomposites. In J.B. Holt, M. Koizumi, T. Hirai and Z.A. Munir (eds.) *Proceedings of the Second International Symposium on Functionally Gradient Materials*, vol. 34 of *Ceramic Transactions*. The American Ceramic Society, Westerville, Ohio, pp. 11–20.

Hori, M. and Vaikuntan, N. (1997). Rigorous formulation of crack path in two-dimensional elastic body. *Mechanics of Materials* **26**(1), 1–14.

Hussain, M.A., Pu, S.L. and Underwood, J. (1974). Strain energy release rate for a crack under combined mode I and mode II. In P.C. Paris and G.R. Irwin (eds.), *Fracture Analysis*, ASTM STP 560. American Society for Testing and Materials, Philadelphia, PA, pp. 2–28.

Ilschner, B. (1996). Processing-microstructure-property relationships in graded materials. *Journal of the Mechanics and Physics of Solids* **44**(5), 647–656.

Kanninen, M.F. and Popelar, C.H. (1985). *Advanced Fracture Mechanics*. Oxford University Press, New York.

Khan, S.M.A. and Khraisheh, M.K. (2004). A new criterion for mixed mode fracture initiation based on the crack tip plastic core region. *International Journal of Plasticity* **20**(1), 55–85.

Kim, J.-H. (2003). Mixed-mode crack propagation in functionally graded materials. Ph.D. Thesis, University of Illinois at Urbana-Champaign, Illinois.

Kim, J.-H. and Paulino, G.H. (2002a). Finite element evaluation of mixed-mode stress intensity factors in functionally graded materials. *International Journal for Numerical Methods in Engineering* **53**(8), 1903–1935.

Kim, J.-H. and Paulino, G.H. (2002b). Isoparametric graded finite elements for nonhomogeneous isotropic and orthotropic materials. *Journal of Applied Mechanics, Transactions ASME* **69**(4), 502–514.

Kim, J.-H. and Paulino, G.H. (2003a). T-stress, mixed-mode stress intensity factors, and crack initiation angles in functionally graded materials: A unified approach using the interaction integral method. *Computer Methods in Applied Mechanics and Engineering* **192**(11–12), 1463–1494.

Kim, J.-H. and Paulino, G.H. (2003b). An accurate scheme for mixed-mode fracture analysis of functionally graded materials using the interaction integral and micromechanics models. *International Journal for Numerical Methods in Engineering* **58**(10), 1457–1497.

Knowles, J.K. and Sternberg, E. (1972). On a class of conservation laws in linearized and finite elastostatics. *Archive for Rational Mechanics and Analysis* **44**(2), 187–211.

Konda, N. and Erdogan, F. (1994). The mixed mode crack problem in a nonhomogeneous elastic medium. *Engineering Fracture Mechanics* **47**(4), 533–545.

Kurihara, K., Sasaki, K. and Kawarada, M. (1990). Adhesion improvement of diamond films. In M. Yamanouochi, M. Koizumi, T. Hirai and I. Shiota (eds.) *Proceedings of the First International Symposium on Functionally Gradient Materials*, Tokyo, Japan.

Lambros, J., Cheeseman, B.A. and Santare, M.H. (2000). Experimental investigation of the quasi-static fracture of functionally graded materials. *International Journal of Solids and Structures* **37**(27), 3715–3732.

Lee, Y.-D. and Erdogan, F. (1995). Residual/thermal stresses in FGM and laminated thermal barrier coatings. *International Journal of Fracture* **69**(2), 145–165.

Lin, C.Y., McShane, H.B. and Rawlings, R.D. (1994). Structure and properties of functionally gradient aluminium alloy 2124/SiC composites. *Materials Science and Technology* **10**(7), 659–664.

Moon, R.J., Hoffman, M., Hilden, J., Bowman, K.J., Trumble, K.P. and Rodel, J. (2002). R-curve behavior in alumina–zirconia composites with repeating graded layers. *Engineering Fracture Mechanics* **69**(14–16), 1647–1665.

Palaniswamy, K. and Knauss, W.G. (1978). On the problem of crack extension in brittle solids under general loading. In S. Nemat-Nasser (ed.) *Mechanics Today*, vol. 4. Pergamon Press, Oxford, pp. 87–148.

Paulino, G.H., Jin, Z.H. and Dodds, R.H. Jr., (2003). Failure of functionally graded materials. In B. Karihaloo and W.G. Knauss, (eds.), *Comprehensive Structural Integrity*. vol. 2, Chapter 13, pp. 607–644, Elsevier Science.

Paulino, G.H., Menezes, I.F.M., Neto, J.B.C. and Martha, L.F. (1999). A methodology for adaptive finite element analysis: towards an integrated computational environment. *Computational Mechanics* **23**(5–6), 361–388.

Rao, B.N. and Rahman, S. (2003). Mesh-free analysis of cracks in isotropic functionally graded materials. *Engineering Fracture Mechanics* **70**(1), 1–27.

Rice, J.R. (1968). A path-independent integral and the approximate analysis of strain concentration by notches and cracks. *Journal of Applied Mechanics, Transactions ASME* **35**(2), 379–386.

Rousseau, C.-E. and Tippur, H.V. (2000). Compositionally graded materials with cracks normal to the elastic gradient. *Acta Materialia* **48**(16), 4021–4033.

Sih, G.C. (1974). Strain energy density factor applied to mixed mode crack problems. *International Journal of Fracture* **10**(3), 305–321.

Suresh, S. and Mortensen, A. (1998). *Fundamentals of Functionally Graded Materials*. IOM Communications Ltd, London.

Wasiluk, B. and Golos, K. (2000). Prediction of crack growth direction under plane stress for mixed-mode I and II loading. *Fatigue and Fracture of Engineering Materials and Structures* **23**(5), 381–386.

Wawrzynek, P.A. (1987). Interactive finite element analysis of fracture processes: an integrated approach. M.S. Thesis, Cornell University.

Wawrzynek, P.A. and Ingraffea, A.R. (1991). Discrete modeling of crack propagation: theoretical aspects and implementation issues in two and three dimensions. Report 91-5, School of Civil Engineering and Environmental Engineering, Cornell University.

Williams, M.L. (1957). On the stress distribution at the base of a stationary crack. *Journal of Applied Mechanics, Transactions ASME* **24**(1), 109–114.

Yau, J.F., Wang, S.S. and Corten, H.T. (1980). A mixed-mode crack analysis of isotropic solids using conservation laws of elasticity. *Journal of Applied Mechanics, Transactions ASME* **47**(2), 335–341.